Available online at www.sciencedirect.com
ScienceDirect
Journal of Sound and Vibration 320 (2009) 43–59
JOURNAL OF SOUND AND VIBRATION
www.elsevier.com/locate/jsvi

Reduction of flow-induced vibration and noise of an optical disk drive

C.C. Cheng*, F.T. Wu, K.L. Ho

Department of Mechanical Engineering, National Chung Cheng University, Chia-Yi, 621 Taiwan, ROC

Received 20 October 2006; received in revised form 17 February 2008; accepted 2 August 2008
Handling Editor: L.G. Tham
Available online 19 September 2008

Abstract

With the increased demands in performance, the optical disk drive needs to have high speed, be more stable and less noisy. However, the disk vibration and the associate noise induced by the rotating flow caused by fluid–structure interactions become more severe as the rotating speed of the disk drive increases. The purpose of this research is to design a disk cover of an optical disk drive that can effectively improve the flow-induced disk vibration and the associate noise as the rotating speed of the disk increases. Numerical results from the finite-element analysis show that altering the shape of disk top cover influences the rotating flow and the corresponding secondary recirculating vortex, and then affects the disk vibration. With a proper design of a disk cover, the flow-induced disk vibration can be reduced substantially as compared to the original shape of the top cover at a rotating speed of 8000 rev/min. Furthermore, experimental results show that the associate noise that includes the flow noise and structure-borne noise of disk can be reduced at least 10 dB at the same rotating speed.

1. Introduction

Increasing the data storage capacity of an optical disk accompanied by the demands of high data access rates and high positioning accuracy of read/write heads has recently become a stringent necessity. With the increased demands in performance, the optical disk drive needs to be rotating with high speed and more stable. However, considerable vibration problems become apparent as the increase of the optical disk rotating speed. For a high-speed disk drive, the flutter caused by fluid–structure interactions becomes apparent and leads to track misregistration. The spinning disk vibrations or the flow-induced disk vibrations have attracted considerable attention and have been investigated numerically and experimentally [1–8]. The rotating disk induces a whirling motion of the fluid in the gap between shroud and disk due to viscosity. A pressure field then is generated to balance the centrifugal and Coriolis forces acting on the fluid particles. Two typical flows are produced: the flow in the disk rotation direction, called the primary flow and that perpendicular to the disk surface, called the secondary flow. The fluid near the cover has a low speed and spirals inward whereas the fluid near the disk has a higher speed and spirals outward. Under the circumstances, a radial inflow near the

*Corresponding author. Tel.: +886 5 2720411x33313; fax: +886 5 2720589.
E-mail address: imeccc@ccu.edu.tw (C.C. Cheng).

0022-460X/$ - see front matter © 2008 Elsevier Ltd. All rights reserved.
doi:10.1016/j.jsv.2008.08.007

cover and a radial outflow near the disk are generated. As the disk rotating speed increases, the secondary flow behaves more like a vortex. The convection coupling effect between the radial and axial velocities induced by these vortices strongly enhances the disk flutter. Shimizu et al. [6] indicated that the disk vibration is strongly coupled with the aerodynamic force, which causes the positioning error of the read/write head. Imai [7] showed that the disk flutter is induced by the flow in the disk rotating direction; the azimuthal or primary flow, instead of the airflow perpendicular to the disk. Furthermore, decreasing the disk-to-shroud spacing that effectively restricts the winding of the flow could reduce the pressure fluctuation as well as the disk flutter. Thus it is reasonable to presume that the pressure inside the disk drive cavity associated with different top cover configuration is different. Thus the disk response will be varied if a different disk top cover is used. The purpose of this research is to predict the fluid-induced disk response using different disk top cover when the disk drive is rotating at a high speed.

2. Formulation of a rotating annular disk

Consider a thin, annular disk of thickness h, flexural rigidity $D = Eh^3/12(1-v^2)$, Poisson's ratio v, density ρ_d rotating at a constant angular velocity Ω_z as shown in Fig. 1. When the disk is rotating, the energies in the disk including the strain energy U_B and kinetic energy T_B due to bending; and the strain energy U_R and kinetic energy T_R due to rotation are expressed in the rotating cylindrical coordinates (r, θ, z) as follows [10]:

$$U_B = \frac{D}{2}\iint\left\{\left(\frac{\partial^2 w}{\partial r^2}+\frac{1}{r}\frac{\partial w}{\partial r}+\frac{1}{r^2}\frac{\partial^2 w}{\partial \theta^2}\right)^2 - 2(1-v)\frac{\partial^2 w}{\partial r^2}\left(\frac{1}{r}\frac{\partial w}{\partial r}+\frac{1}{r^2}\frac{\partial^2 w}{\partial \theta^2}\right) + 2(1-v)\left[\frac{\partial}{\partial r}\left(\frac{1}{r}\frac{\partial w}{\partial \theta}\right)\right]^2\right\} r\,\mathrm{d}\theta\,\mathrm{d}r, \tag{1}$$

$$T_B = \frac{\rho_d h}{2}\iint\left(\frac{\partial w}{\partial t}\right)^2 r\,\mathrm{d}r\,\mathrm{d}\theta, \tag{2}$$

$$U_R = \frac{h}{2}\iint\left[\sigma_r\left(\frac{\partial w}{\partial r}\right)^2 + \sigma_\theta\frac{1}{r^2}\left(\frac{\partial w}{\partial \theta}\right)^2\right] r\,\mathrm{d}r\,\mathrm{d}\theta, \tag{3}$$

$$T_R = \frac{\rho_d h}{2}\iint\left[\Omega_z^2\frac{\partial w}{\partial \theta}+2\Omega_z\frac{\partial w}{\partial \theta}\frac{\partial w}{\partial t}\right] r\,\mathrm{d}r\,\mathrm{d}\theta, \tag{4}$$

where w is the disk transverse displacement, σ_r and σ_θ are the normal stresses in the radial and tangential directions, respectively. Note that σ_r and σ_θ are functions of Ω_z and can be determined by solving the following

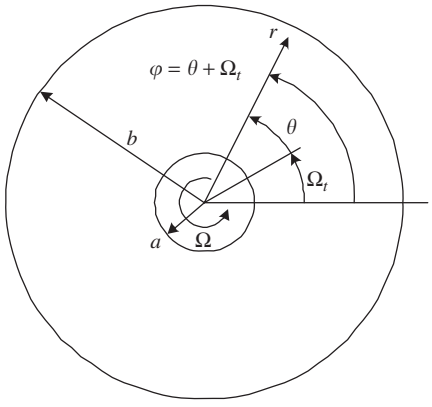

Fig. 1. Schematic diagram of the disk and rotating coordinate system.

equations:

$$\frac{\mathrm{d}}{\mathrm{d}r}r\sigma_r - \sigma_\theta + \rho_d\Omega_z^2 r^2 = 0, \tag{5a}$$

$$r\frac{\mathrm{d}}{\mathrm{d}r}\varepsilon_\theta - \varepsilon_r + \varepsilon_\theta = 0, \tag{5b}$$

where ε_r and ε_θ are the normal strains in the radial and tangential directions, respectively. Using Hamilton's principle, one can derive the governing equation for the forced vibration of the rotating disk subjected to a pressure field in the rotating frame of reference as

$$\rho_d h\left[\frac{\partial^2 w}{\partial t^2} + 2\Omega_z\frac{\partial^2 w}{\partial\theta\partial t} + \Omega_z^2\frac{\partial^2 w}{\partial\theta^2}\right] + D\nabla^4 w - \frac{h}{r}\left[\frac{\partial}{\partial r}\left(\sigma_r r\frac{\partial w}{\partial r}\right) + \frac{\partial}{r\partial\theta}\left(\sigma_\theta\frac{\partial w}{\partial\theta}\right)\right] = p(r,\theta,t), \tag{6}$$

where $p(r, \theta, t)$ is the pressure acting on the disk, $\nabla^2 = \partial^2/\partial r^2 + \partial/r\partial r + \partial^2/\partial r^2\partial\theta^2$ is Laplacian operator and $\nabla^4 = \nabla^2\nabla^2$ is Biharmonic operator. The disk is clamped at the inner radius, $r = a$, and free at the outer radius, $r = b$, so the geometric and natural boundary conditions are expressed respectively as follows:

$$[w(r,\theta,t)]_{r=a} = 0, \quad \left[\frac{\partial}{\partial r}w(r,\theta,t)\right]_{r=a} = 0, \tag{7a, b}$$

$$\left[\frac{\partial^2 w}{\partial r^2} + v\left(\frac{1}{r}\frac{\partial w}{\partial r} + \frac{1}{r^2}\frac{\partial^2 w}{\partial\theta^2}\right)\right]_{r=b} = 0, \tag{7c}$$

$$\left[\frac{\partial}{\partial r}\left(\frac{\partial^2 w}{\partial r^2} + \frac{\partial w}{r\partial r} + \frac{1}{r^2}\frac{\partial^2 w}{\partial\theta^2}\right) + \frac{1-v}{r^2}\frac{\partial^2}{\partial\theta^2}\left(\frac{\partial w}{\partial r} - \frac{w}{r}\right)\right]_{r=b} = 0. \tag{7d}$$

The forced vibration of the rotating disk to Eq. (6) is discretized using the finite-element method and can be expressed as

$$\mathbf{M}\ddot{\mathbf{x}} + \mathbf{G}\dot{\mathbf{x}} + (\mathbf{K}_0 + \mathbf{K}_\sigma - \mathbf{K}_C)\mathbf{x} = \mathbf{p}. \tag{8}$$

In Eq. (8), the gyroscopic matrix $\mathbf{G}(\Omega_z)$ is due to Coriolis effect and the stress stiffening matrix $\mathbf{K}_\sigma(\Omega_z)$ and the spinning softening matrix $\mathbf{K}_C(\Omega_z)$ are caused by the centrifugal effects [14].

3. Formulation of a rotating flow in an enclosure

In this section, equations are introduced for describing the rotational effect in rotating flow. The equations were cited from Refs. [11–13] which describe the rotating flow, Navier–Stokes and k–ε equations, and rotating turbulence models, respectively. Similar equations for general fluid dynamics analysis can also be found in ANSYS [17]; however, the main equations in this section are narrowed down to describing the rotational effect of a rotating flow.

The enclosure geometry, fluid properties and flow speed dominate the flow pattern in an enclosure. One can determine the type of flow, i.e. the laminar or turbulent flow, based on the Reynolds number. For a disk rotating with a high speed, the statistical technique is required to characterize the turbulent flow due to variations of physic quantities in the temporal and spatial domains. The effect of temporal variations, e.g. velocity fluctuations, can be eliminated using the Reynolds average (time average); and the effect of spatial variations, e.g. density fluctuations, can be excluded using the Favre average (mass-weighted average). Consider the fluid of density ρ and viscosity μ confined in a disk enclosure as shown in Fig. 2. The continuity and momentum equations of the rotating fluid in a rotating frame of reference are [11]

$$\frac{\partial\rho}{\partial t} + \nabla\cdot(\rho\mathbf{u}) = 0, \tag{9a}$$

$$\frac{\partial(\rho\mathbf{u})}{\partial t} + \nabla\cdot(\rho\mathbf{u}\otimes\mathbf{u}) = \nabla\cdot(-p\delta + \mu(\nabla\mathbf{u} + (\nabla\mathbf{u})^{\mathrm{T}})) + \mathbf{f}, \tag{9b}$$

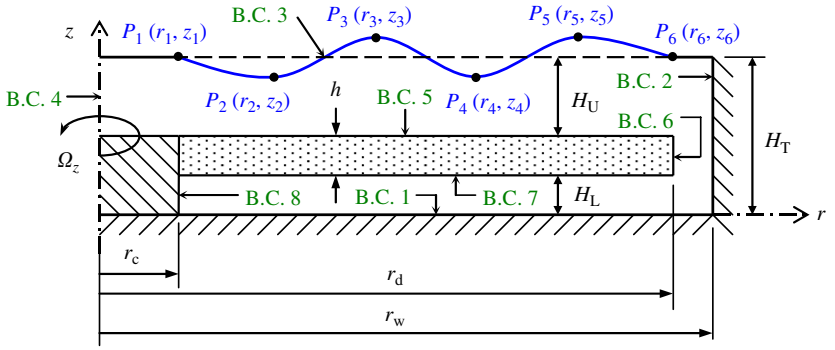

Fig. 2. Schematic diagram of a simplified disk drive.

where the instantaneous velocity vector $\mathbf{u} = u_x\mathbf{i} + u_y\mathbf{j} + u_z\mathbf{k}$ and pressure p are the system variables of Eq. (9) in the rotating coordinates. The body force vector $\mathbf{f}$ due to rotation in Eq. (9b) consists of Coriolis and the centrifugal force:

$$\mathbf{f} = -2\rho\boldsymbol{\Omega} \times \mathbf{u} - \rho\boldsymbol{\Omega} \times (\boldsymbol{\Omega} \times \mathbf{R}), \tag{10}$$

where $\boldsymbol{\Omega} = \Omega_x\mathbf{i} + \Omega_y\mathbf{j} + \Omega_z\mathbf{k}$ is the rotating velocity vector and $\mathbf{R}$ stands for the position vector.

The instantaneous velocity u_i of the flow can be expressed as the sum of the averaged mean component $\bar{u}_i$ and a fluctuating component u_i'. Consequently, the mass-weighted time-averaged Navier–Stokes equations for a turbulent flow system are given as follows [12]:

$$\frac{\partial \bar{\rho}}{\partial t} + \frac{\partial}{\partial x_j}(\bar{\rho}\tilde{u}_j) = 0, \tag{11a}$$

$$\frac{\partial}{\partial t}(\bar{\rho}\tilde{u}_i) + \frac{\partial}{\partial x_j}(\bar{\rho}\tilde{u}_j\tilde{u}_i) = \frac{\partial}{\partial x_j}\left[-\bar{p}\delta_{ij} + \mu\left(\frac{\partial \tilde{u}_i}{\partial x_j} + \frac{\partial \tilde{u}_j}{\partial x_i}\right) - \overline{\rho u_i' u_j'}\right] + f_i, \tag{11b}$$

where $\overline{\rho u_i' u_j'}$ is the Reynolds stress tensor, δ_{ij} is the Kronecker delta and $\tilde{u}_i = \overline{\rho u_i}/\bar{\rho}$ is the mass-weighted time-averaged velocity. With the unknown correlation terms in the Reynolds stress tensor, it is required to model the Reynolds stress by additional equations of known quantities in order to obtain a closed set of partial differential equations. To address this problem, the familiar two-equation k–ε closure system involving two differential transport equations for the turbulence kinetic energy k and turbulence dissipation rate ε can be utilized. The standard k–ε equations are expressed as follows [12]:

$$\frac{\partial}{\partial t}(\bar{\rho}k) + \frac{\partial}{\partial x_j}\left[\bar{\rho}\tilde{u}_j k + \left(C_k\overline{\rho u_i' u_j'}\frac{k}{\varepsilon} - \mu\delta_{ij}\right)\frac{\partial k}{\partial x_i}\right] + \overline{\rho u_i' u_j'}\frac{\partial \tilde{u}_i}{\partial x_j} + \bar{\rho}\varepsilon = 0, \tag{12a}$$

$$\frac{\partial}{\partial t}(\bar{\rho}\varepsilon) + \frac{\partial}{\partial x_j}\left[\bar{\rho}\tilde{u}_j\varepsilon + \left(C_\varepsilon\overline{\rho u_i' u_j'}\frac{k}{\varepsilon}\right)\frac{\partial \varepsilon}{\partial x_i}\right] + C_{\varepsilon 1}\overline{\rho u_i' u_j'}\frac{\varepsilon}{k}\frac{\partial \tilde{u}_i}{\partial x_j} + C_{\varepsilon 2}\bar{\rho}\frac{\varepsilon^2}{k} = 0, \tag{12b}$$

where C_k, C_ε, $C_{\varepsilon 1}$ and $C_{\varepsilon 2}$ are constants. For some extensions or modifications of the k–ε model, the Reynolds stress is related to the diffusion terms using $-\mu_t(\partial\tilde{u}_i/\partial x_j + \partial\tilde{u}_j/\partial x_i)$, thus Eq. (11b) can be rewritten as

$$\frac{\partial}{\partial t}(\bar{\rho}\tilde{u}_i) + \frac{\partial}{\partial x_j}(\bar{\rho}\tilde{u}_j\tilde{u}_i) = \frac{\partial}{\partial x_j}\left[-\bar{p}\delta_{ij} + \mu_e\left(\frac{\partial \tilde{u}_i}{\partial x_j} + \frac{\partial \tilde{u}_j}{\partial x_i}\right)\right] + f_i, \tag{13}$$

where the effective viscosity $\mu_e = \mu + \mu_t$ consists of the laminar viscosity μ and the turbulent viscosity μ_t. Each extended k–ε model offers different constant C_μ and the source term in the dissipation equation, hence the turbulent viscosity $\mu_t = C_\mu\rho k^2/\varepsilon$ is calculated with the C_μ and the solution to the turbulence equations (12).

In this paper, the Girimaji (GIR) model provided by ANSYS FLOTRAN is employed to deal with the rotating turbulence [13]. The GIR turbulence model is a k–ε based Reynolds stress model and is proper to simulate strongly swirling flows with secondary vortices resulting from the anisotropy of the Reynolds stresses.

Following Ref. [13], the GIR turbulence model is a fully-explicit and self-consistent algebraic Reynolds stress model. In addition to the continuity, momentum and turbulence equations, six algebraic equations for Reynolds stresses and two invariants are introduced to calculate the C_μ. The symmetric deformation tension S_{ij} and antisymmetric rotation tension W_{ij} are utilized to construct the two invariants η_1 and η_2:

$$S_{ij} = \frac{1}{2}\left(\frac{\partial u_i}{\partial x_j} + \frac{\partial u_j}{\partial x_i}\right), \tag{14a}$$

$$W_{ij} = \frac{1}{2}\left(\frac{\partial u_i}{\partial x_j} - \frac{\partial u_j}{\partial x_i}\right) + C_r e_{ijk}\Omega_k, \tag{14b}$$

$$\eta_1 = \frac{k}{\varepsilon}\sqrt{2S_{ij}S_{ij}}, \tag{14c}$$

$$\eta_2 = \frac{k}{\varepsilon}\sqrt{2W_{ij}W_{ij}}, \tag{14d}$$

where C_r is a given rotational constant, e_{ijk} is alternating tensor operator and Ω_k is the rotating velocity vector of the rotating frame of reference. Therefore, the effective viscosity $\mu_t = \mu_t(k, \varepsilon, S_{ij}, W_{ij})$ is a function of k, ε, S_{ij} and W_{ij}.

For discretization of the governing equations (12) and (13), Galerkin's method of weighted residual is utilized [12]. Then, the assembled system equations for variables u_i, k and ε to the rotating turbulence can be expressed as

$$\mathbf{A}_\phi \boldsymbol{\phi} = \mathbf{S}_\phi, \tag{15}$$

where ϕ expresses each system variable, $\mathbf{S}_\phi$ is the source term and the system matrix $\mathbf{A}_\phi$ consists of the transient, advection and diffusion terms. In discretization of the advection effect, the second-order upwind scheme, the Streamline Upwind/Petro-Galerkin approach, is employed [15].

The transient velocity and pressure response of the rotating turbulent flow can be determined using the Semi-Implicit Method for Pressure-Linked Equations (SIMPLE) coupling algorithms to solve the system equation (15) [9]. To overcome the unstable nature in a typical turbulence problem during the numerical calculation, the Successive Over-Relaxation (SOR) method which utilizes a relaxation factor is adopted:

$$\phi'^{q+1} = \phi'^{q} + R_\phi(\phi^{q+1} - \phi'^{q}), \tag{16}$$

where R_ϕ is the relaxation factor, q is the iteration number and ϕ with the superscript "′" represents the degree of freedom obtained using the relaxation factor. To avoid numerical divergence during the calculation, a conservative but time-consuming under-relaxation factor $R_\phi = 0.5$ is used in the numerical simulation. The overall convergence is measured in each iteration based on the normalized ratio test defined between two successive iterations:

$$\sum_{i=1}^{N}\left|\phi_i'^{q+1} - \phi_i'^{q}\right| \Big/ \sum_{i=1}^{N}\left|\phi_i'^{q+1}\right| < \varepsilon_\phi, \tag{17}$$

where ε_ϕ is the value designated for the criterion of convergence and N is the total number of the finite-element nodes.

4. Dynamic coupling between a rotating disk and a fluid flow

For a disk rotating in an enclosure as shown in Fig. 2, the fluid pressure induced by the rotating disk will also act as a feedback force exerting on the disk. The dynamic coupling between the spinning disk and the corresponding induced flow will be enhanced as the disk rotating speed increases. For an extremely small time duration Δt, one can obtain the pressure distribution while neglecting the disk deformation; and then solve the disk response while assuming that the pressure is changed linearly for the next Δt. The procedure for the linearized fluid–structure interaction is shown in Fig. 3. However, the numerical convergence strongly depends

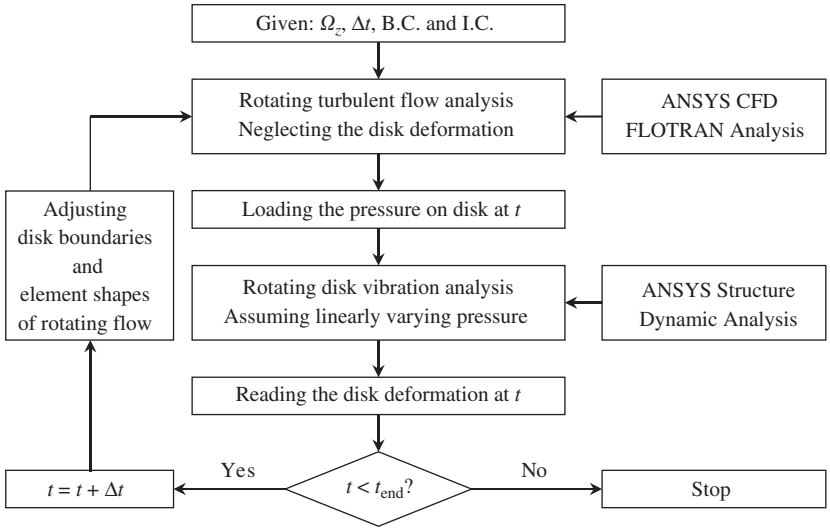

Fig. 3. Linearized fluid–structure interaction.

on the magnitude of time interval Δt in such a computation-intensive process. A numerical algorithm, which incorporates commercial structural analysis code ANSYS, mathematical subroutines IMSL libraries and the user-supplied routines is proposed. The advantage is simply that it extends the capability and flexibility of ANSYS. ANSYS calculates the pressure and velocity distribution in a complicate enclosure, the dynamic response of the disk, etc., whereas IMSL is responsible for providing subroutines including optimization, transformations, matrix operations, etc. The user-supplied subroutine is required not only for the interface between IMSL and ANSYS but also controlling the iteration in a transient analysis or in an optimization procedure. The computation is intensive and time consuming; thus one can code the rotating disk himself instead of using ANSYS for the vibration analysis in order to save time due to its simple geometry. In other words, this algorithm provides a general and an automatic procedure to handle a multidisciplinary problem.

5. Numerical simulations

In order to study the influences of the aerodynamic force of the flow on the disk response, numerical simulations of a flow enclosed in a co-axial circular shroud with a disk rotating inside as shown in Fig. 2 were performed in the rotating coordinate system. Only half of the model is used in the finite-element analysis, so one can observe only the axial symmetric response of the disk. However, the three-dimensional axisymmetric flow model, which has assumptions of incompressible, adiabatic and Newtonian fluid, possesses not only the radial velocity u_r and axial velocity u_z but also the swirling degree-of-freedom u_θ. The dimension and material properties are listed in Table 1 and the boundary conditions of the flow in the rotating coordinate system are listed in Table 2. The numerical simulations were carried out on a disk of 120 mm in diameter, 1.2 mm in thickness and rotating at a constant speed Ω_z.

5.1. Steady-state analysis of rotating turbulent flow driven by a rigid disk

In Ref. [18], two kinds of rotating flow were introduced. One is a flow driven by a rotating disk, and the other is a rotating flow over a fixed disk. With an axisymmetric model, exact solutions to the Navier–Stokes equations can be obtained with two kinds of boundary layer near the rotating disk and the fixed disk, respectively. The boundary layer near the rotating disk is called Ekman layer, and the layer near the fixed disk is called Bodewadt layer. The interactions between these two kinds of rotating flow were investigated by experiments of the Reynolds number ranged from 10^3 to 10^5 [11]. The Ekman boundary layer near the rotating disk is acting as a pump centrifuging the fluid outward the lateral shroud, and the Bodewadt boundary layer near the top cover and bottom shroud guide the fluid inward to the rotating axis. Then, a

Table 1
Dimension and material properties of a disk drive

r_c	15×10^{-3} m	E	2.16 GPa
r_d	60×10^{-3} m	H_U	6.2×10^{-3} m
r_w	62×10^{-3} m	H_L	4.0×10^{-3} m
h	1.2×10^{-3} m	ρ	1.205 kg/m^3
ρ_d	1200 kg/m^3	μ	1.8135×10^{-5} kg/m s
v	0.38		

Table 2
Boundary conditions of flow in the rotating coordinate system

B.C.	Velocity boundary condition	Description
1–3	$u_r = u_z = 0$ and $u_\theta = -r\Omega_z$	Fixed shroud
4	$u_r = u_\theta = 0$	Axisymmetric axis
5–8	$u_r = u_z = u_\theta = 0$	Rotating disk

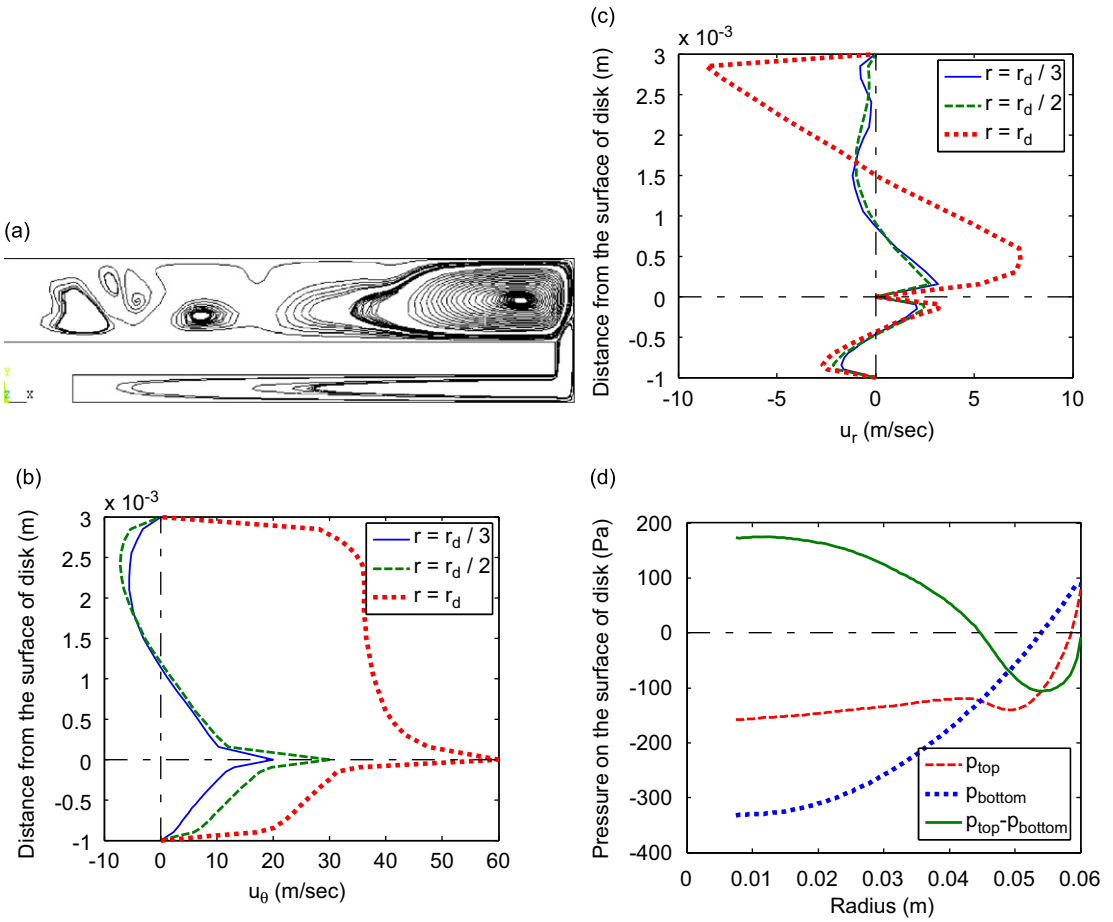

Fig. 4. Steady-state rotating turbulence with a rigid disk rotating at 1000 rad/s: (a) stream function, (b) swirling velocity, (c) radial velocity and (d) surface pressure.

secondary flow is developed near the lateral shroud due to the interaction of Ekman and Bodewadt boundary layers.

The Reynolds number, $Re = \rho\Omega_z r_w^2/\mu$, and the aspect ratio, H_U/r_w or H_L/r_w, in Fig. 2 determine whether the rotating flow turns into turbulence. In order to study the effects of the rotating turbulence, a steady-state analysis of the flow with a rigid disk rotating inside an enclosure with a flat top cover was performed. With $\Omega_z = 1000$ rad/s (9550 rev/min), $H_U = 3.0 \times 10^{-3}$ m, $H_L = 1.0 \times 10^{-3}$ m and other parameters listed in Table 1, Fig. 4(a) shows the stream function of the flow with the GIR turbulence model at $Re = 2.55 \times 10^5$. For the same Reynolds number, the turbulent effect is obvious in the region over the rotating disk with a large aspect ratio H_U/r_w; while the viscous effect dominates the flow under the disk with a small aspect ratio H_L/r_w, as shown in Fig. 4. The velocity profiles of the primary and secondary flows are shown in Figs. 4(b) and (c), respectively, in different radii. One may notice that the velocities in Fig. 4 were transformed to the stationary coordinate system. Under the rotating disk, the flow seems to be laminar according to the velocity profile, and the pressure on the bottom surface of the disk varies gradually as shown in Fig. 4(d). Nevertheless, the radial pressure gradient on the top surface near the outer rim of the disk changes rapidly. The pressure difference between the top and the bottom surfaces, i.e. the net pressure $p_{\text{top}} - p_{\text{bottom}}$, changes from positive to negative values and it is the main cause for disk deformation.

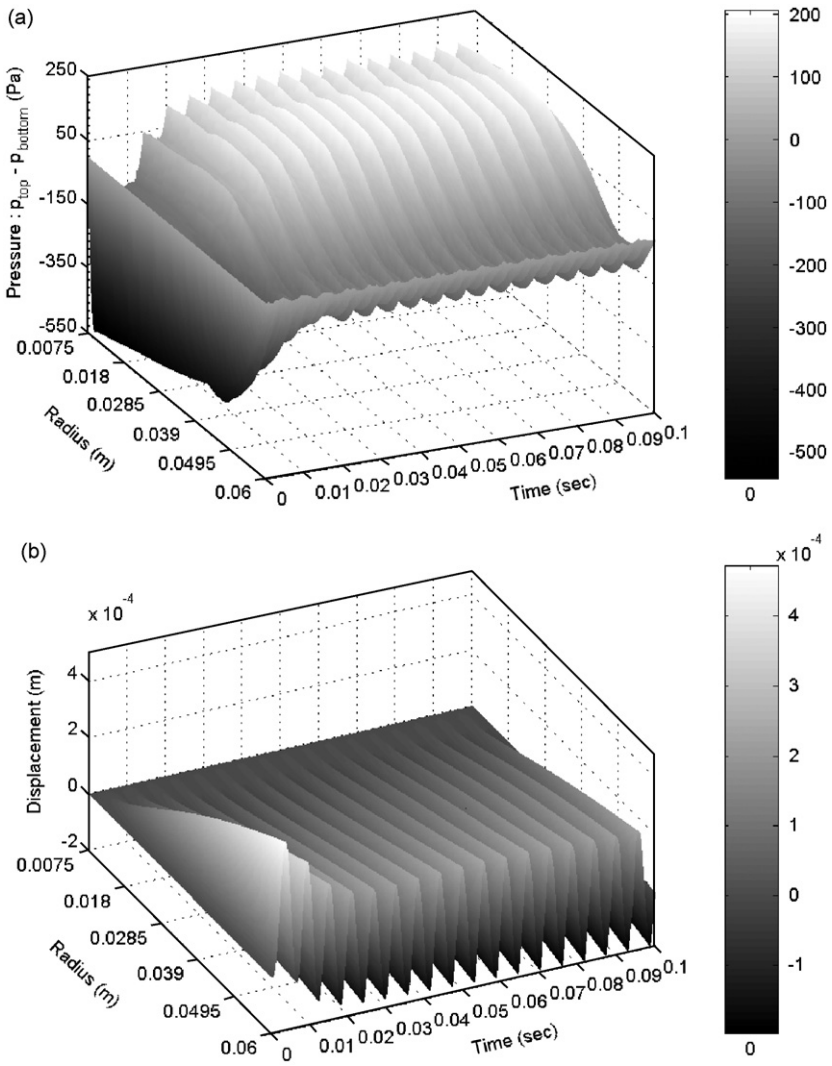

Fig. 5. Transient rotating turbulence with a flexible disk rotating at 1000 rad/s: (a) net pressure oscillation and (b) disk vibration.

5.2. Transient analysis of rotating turbulent flow driven by a flexible disk

The net pressure between the top and the bottom surfaces of the disk results in deformation of the flexible disk and then the deformed disk in the rotating flow alters the pressure distribution due to the change of the boundaries, and vice versa. Therefore, a transient analysis of the rotating turbulent flow excited by a spinning flexible disk is necessary for investigating the coupling effect between the fluid flow and the structure.

Assume the initial conditions to be zero pressure and zero velocities for the rotating flow. The transient analysis of the coupled system for the time duration of 0.1 s was performed. Figs. 5(a) and (b) show the pressure difference between the top and the bottom surfaces; and the displacement response of the disk, respectively. After the time of 0.05 s, the responses of the net pressure and disk displacement become steady;

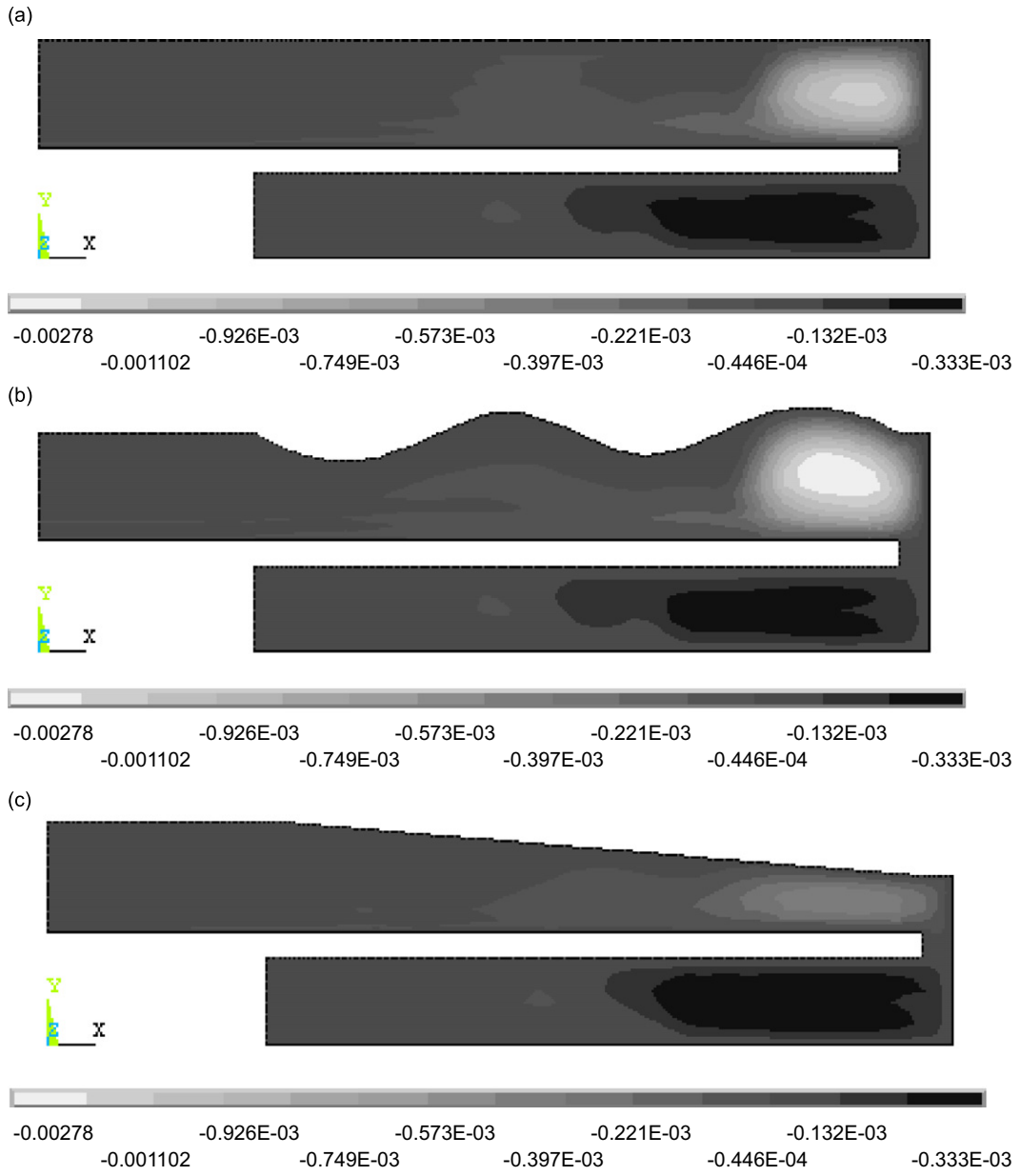

Fig. 6. The streamline distributions at 0.1 s at 8000 rev/min: (a) Cover 1, (b) Cover 2 and (c) Cover 3.

however, they consist of the steady-state and transient components. In Fig. 5(a), the profile of the steady net pressure is similar to that of the steady-state result as shown in Fig. 4(d). It is a typical flow-induced vibration phenomenon that the pressure fluctuation results from the disk vibration, while the flexible disk flutters as it is rotating in the enclosure filled with air.

5.3. Transient rotating turbulence driven by a flexible disk to different covers

Kim [16] studied the air-borne noise experimentally by changing the gap between the disk and the cover of a hard disk drive. In this research, a numerical simulation is performed first and three top covers with different cross sections of an optical disk drive have been chosen to reduce the flow noise. Besides a flat top cover, which is simply referred as the original configuration or Cover 1, two configurations as illustrated in Fig. 6 are considered and are denoted as Cover 2 and Cover 3. The cross sections of Cover 2 and Cover 3 are designed using B-spline curve with control points listed in Table 3. The disk responses from both configurations will be compared to each other and with that of the original configuration.

With $\Omega_z = 8000$ rev/min, $H_U = 6.2 \times 10^{-3}$ m, $H_L = 4.0 \times 10^{-3}$ m and other parameters listed in Table 1, the streamlines and velocity distributions that reveal the flow pattern are shown in Fig. 6(a) for the original top cover at 0.1 s, whereas the streamlines and velocity distributions for Cover 2 and Cover 3 are shown in Figs. 6(b) and (c), respectively. These figures show that the spiral vortex which occurs in the transition region of boundary layer is located near the rim of the disk. Apparently, near the rim of the disk the velocity changes rapidly from a small value at the disk surface to some relatively large value in a very short distance above the disk surface. This rapid change in velocity due to slip results in a large velocity gradient normal to the disk surface, which produces shear stresses and then the vortex even though the viscosity is small. From these figures, it is obvious that the shape of the top cover mainly influences the flow in the radial and the transverse directions; as well as the development of the vortex. The pressure distributions corresponding to each disk top cover are shown in Figs. 7(a)–(c), respectively. The greatest pressure of all occurs at the tip of the disk in three figures. However, after a detailed examination, one may note that the pressure in Cover 3 is distributed much uniformly than the others. Furthermore, the pressure difference between the top and the bottom surfaces in Cover 3 is also the smallest among them.

Under the same operating conditions, the disk transverse displacement at $r = r_d$ corresponding to the original top cover, Cover 2 and Cover 3 are shown in Fig. 8. The displacement response corresponding to Cover 3 is the smallest among them and is approximated 50% lower than of Cover 1, the original cover. When the disk rotating speed reduces to 4000 rev/min, the disk transverse displacement at $r = r_d$ is shown in Fig. 9. It shows that the disk displacement corresponding to Cover 3 is still smaller than that of Cover 1 and the vibration amplitude of the disk with Cover 2 is the smallest. The amplitudes and offsets of the steady responses of the vibration at the disk rim as shown in Figs. 8 and 9 are listed in Table 4. Nevertheless, the result from numerical simulations requires experimental validation which will be illustrated in the next section.

The fundamental natural frequency is 128.50 Hz for the non-rotating disk in a vacuum and is 216.02 Hz when it is rotating at 8000 rev/min. When the disk is rotating, the disk is stretched due to inertia effect and thus its in-plane stiffness increases. Therefore, the disk natural frequency increases as the rotating speed increases.

Table 3
Coordinates of control points used in design of top cover, where $\Delta z = 1.0 \times 10^{-3}$ m

	Cover 2		Cover 3	
	r	z	r	z
P_1	r_c	H_T	r_c	H_T
P_2	$r_c+1(r_d-r_c)/5$	$H_T-\Delta z$	$r_c+1(r_d-r_c)/5$	$H_T-1\Delta z/2$
P_3	$r_c+2(r_d-r_c)/5$	$H_T+\Delta z$	$r_c+2(r_d-r_c)/5$	$H_T-2\Delta z/2$
P_4	$r_c+3(r_d-r_c)/5$	$H_T-\Delta z$	$r_c+3(r_d-r_c)/5$	$H_T-3\Delta z/2$
P_5	$r_c+4(r_d-r_c)/5$	$H_T+\Delta z$	$r_c+4(r_d-r_c)/5$	$H_T-4\Delta z/2$
P_6	r_d	H_T	r_d	$H_T-5\Delta z/2$

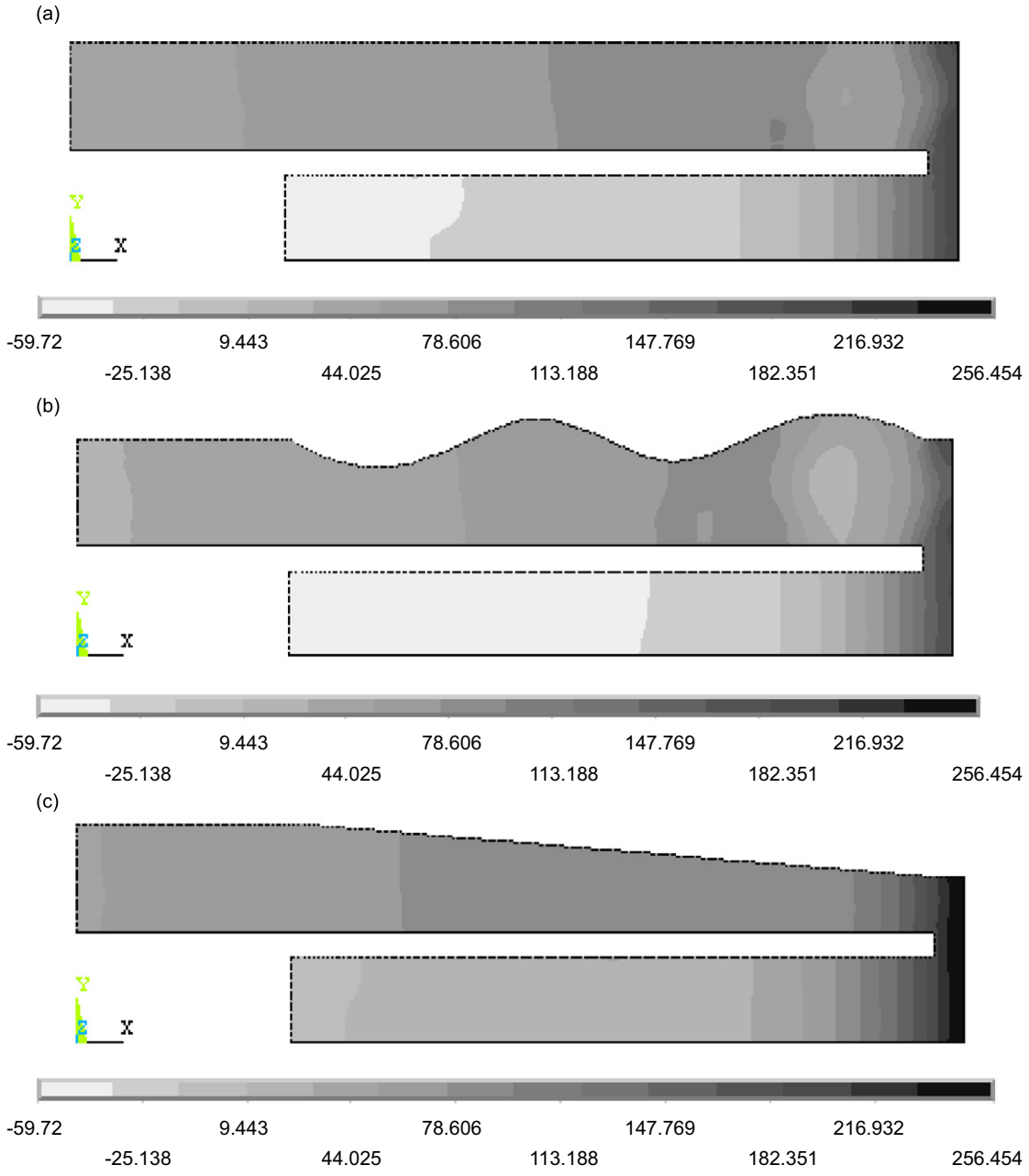

Fig. 7. The pressure distributions at 0.1 s at 8000 rev/min. (a) Cover 1, (b) Cover 2 and (c) Cover 3.

For the rotating disk subject to flow-induced excitation, the disk frequency responses are obtained after applying Fast Fourier Transform (FFT) to the disk displacements as shown in Fig. 8. The disk displacement in each case typically exhibits pure tone excitation with frequencies of 191.95, 191.35 and 199.28 Hz, respectively. It implies that the top cover configuration influences the disk natural frequency due to the added mass effect of fluid, which plays an important role in the disk flow-induced vibration. Moreover, the displacement is obviously dominated by the disk first mode which resembles the first mode of a cantilever and has the greatest displacement at the disk tip. Therefore, it is reasonable to use the disk displacement at its outer rim to represent the disk maximum transverse displacement.

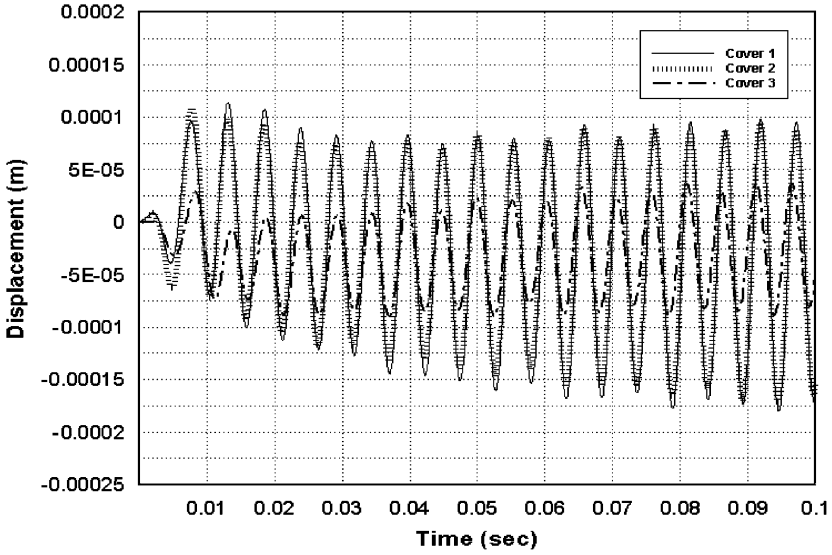

Fig. 8. Comparisons of disk displacement at $r = r_d$ for a disk rotating at 8000 rev/min.

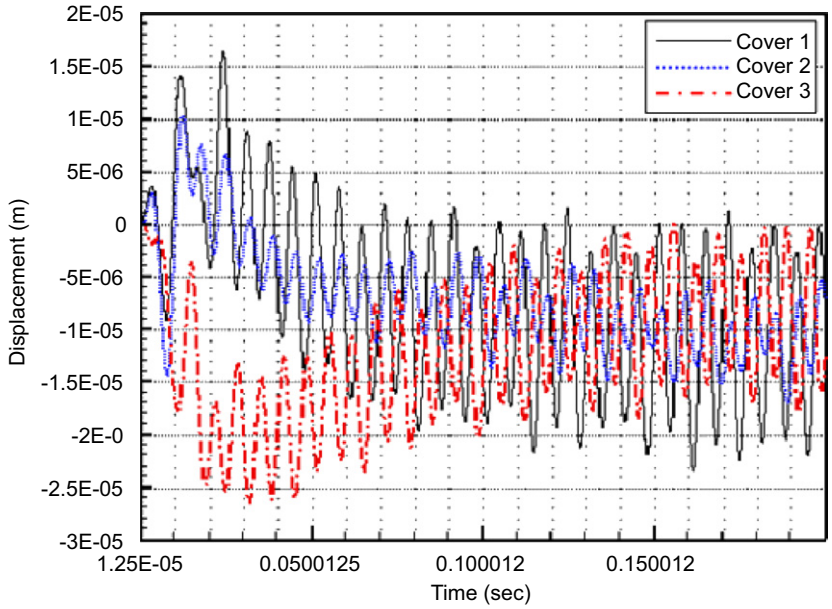

Fig. 9. Comparisons of disk displacement at $r = r_d$ for a disk rotating at 4000 rev/min.

Table 4
Steady responses of the disk vibration in Figs. 8 and 9

Rev/min	Cover 1	Cover 2	Cover 3
8000			
Amplitude (μm)	275	275	125
Offset (μm)	−37.5	−37.5	−25.0
4000			
Amplitude (μm)	25.0	12.0	18.0
Offset (μm)	−12.5	−11.0	−9.0

6. Experimental validations

An experiment was performed to study the influences of the shape of top cover on the disk vibration response and the associate noise while the disk is rotating at a high speed. The experimental setup is shown in Fig. 10. Three disk covers, as shown in Fig. 11, are fabricated using acrylic fibers based on the same designs as those in the numerical simulation. A laser displacement sensor and an infrared tachometer are installed under the ODD. Two small holes were drilled through the bottom of the ODD, so the displacement can be measured at the outer rim of the disk on the side opposite to the top cover as shown in Fig. 12. Note that the hole is on the bottom of the ODD and is as small as possible in order to prevent it from influencing the flow. The sound pressure is measured by a free-field microphone (B&K Type 4190) placed on the same height as the ODD but at a distance of 0.3 m away from it. The disk response at 4000 rev/min is represented by the order spectrum using a FFT analyzer (B&K Type 3560) as shown in Fig. 13. It clearly shows that the disk displacements corresponding to the first three orders dominate the response, which is a typical characteristic of a rotating disk. Moreover, the displacement responses at higher orders for the ODD with top cover are more pronounced than that without top cover. It implies that the top cover enhances the flow agitation and excites high-order modes of the rotating disk.

Table 5 lists the displacement measured at the outer rim of the disk with respective to the ODD without cover and with three different top covers when the disk is rotating, respectively, at 4000, 6000 and 8000 rev/min. The disk displacement of the ODD without cover is also measured to study the influence of the top cover on the disk vibro-acoustic response. The response corresponding to Cover 1, which is a typical, flat top cover, is used as a base line data. It shows that the disk vibration corresponding to the ODD with Cover 3 is the smallest except at 6000 rev/min. On the contrary, the vibration of the ODD with Cover 1 is the worst. Furthermore, the differences in the displacement response between the first and the other orders decrease as the disk rotating speed increases. It shows that the dominance by the first order in the disk displacement

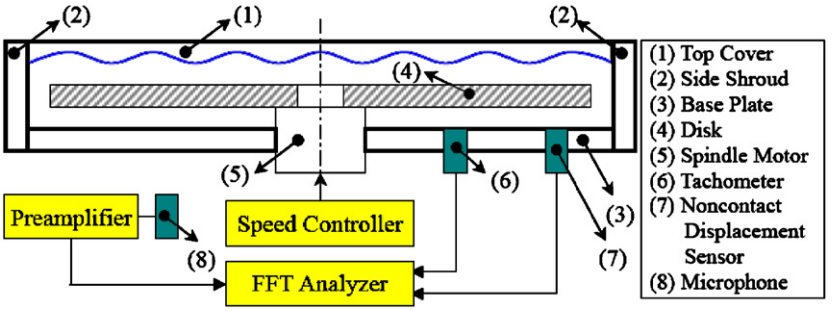

Fig. 10. Schematic diagram of the experimental setup.

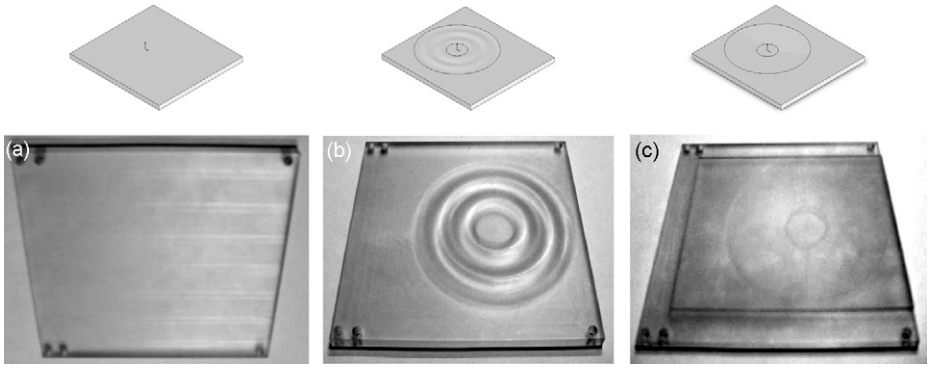

Fig. 11. Three different top covers used in ODD experiments: (a) Cover 1, (b) Cover 2 and (c) Cover 3.

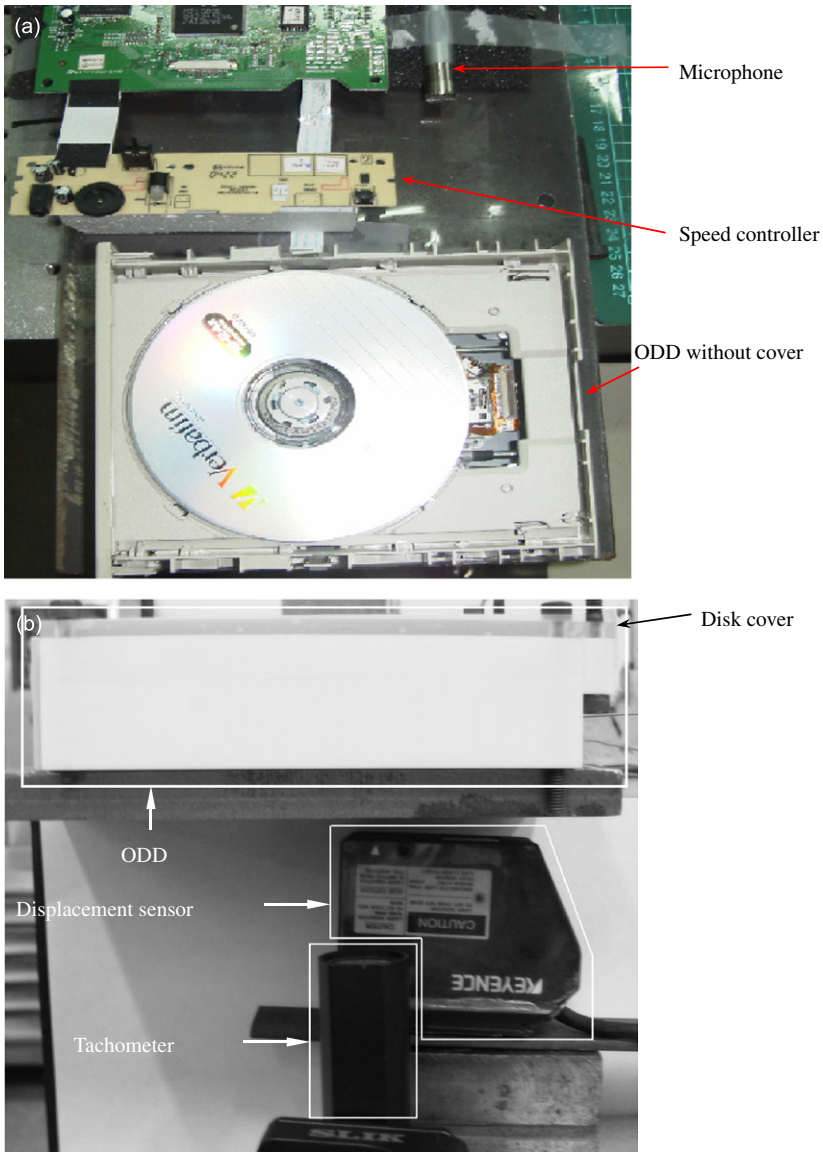

Fig. 12. Displacement measurement of rotating disk: (a) top view and (b) tachometer and displacement are installed below ODD.

response decreases and the rotating flow excites the higher order as the disk rotating speed increases. The sound pressure levels of the ODD without cover and with different covers are listed in Table 6 when the disk is rotating at 8000 rev/min. The sound pressure of the first order of Cover 2 and Cover 3 are, respectively, 19.0 and 12.8 dB smaller than that of Cover 1. Note that the disk acoustic response is represented by the sound pressure order spectrum instead of the total sound pressure level and the experiment is not conducted in an anechoic chamber. The reason is simply that the background noise in the lab did not affect the disk acoustic response at the harmonic orders of the rotating speed due to the little coherence between them. As a general rule, the sound power level instead of sound pressure level should be used in the comparison of disk noise radiation. However, these data are still worthy of being as a reference.

As shown in Fig. 9, when the disk rotational speed is 4000 rev/min (66.67 Hz), the disk vibration frequencies corresponding to the ODD with three covers are approximately 150 Hz after applying FFT to the displacement response. The disk vibration frequency 150 Hz is nearly at 2.25 order of the rotational speed. The amplitudes of the disk with Cover 2 and Cover 3 are smaller than that with Cover 1 in Fig. 9. In Fig. 13 of

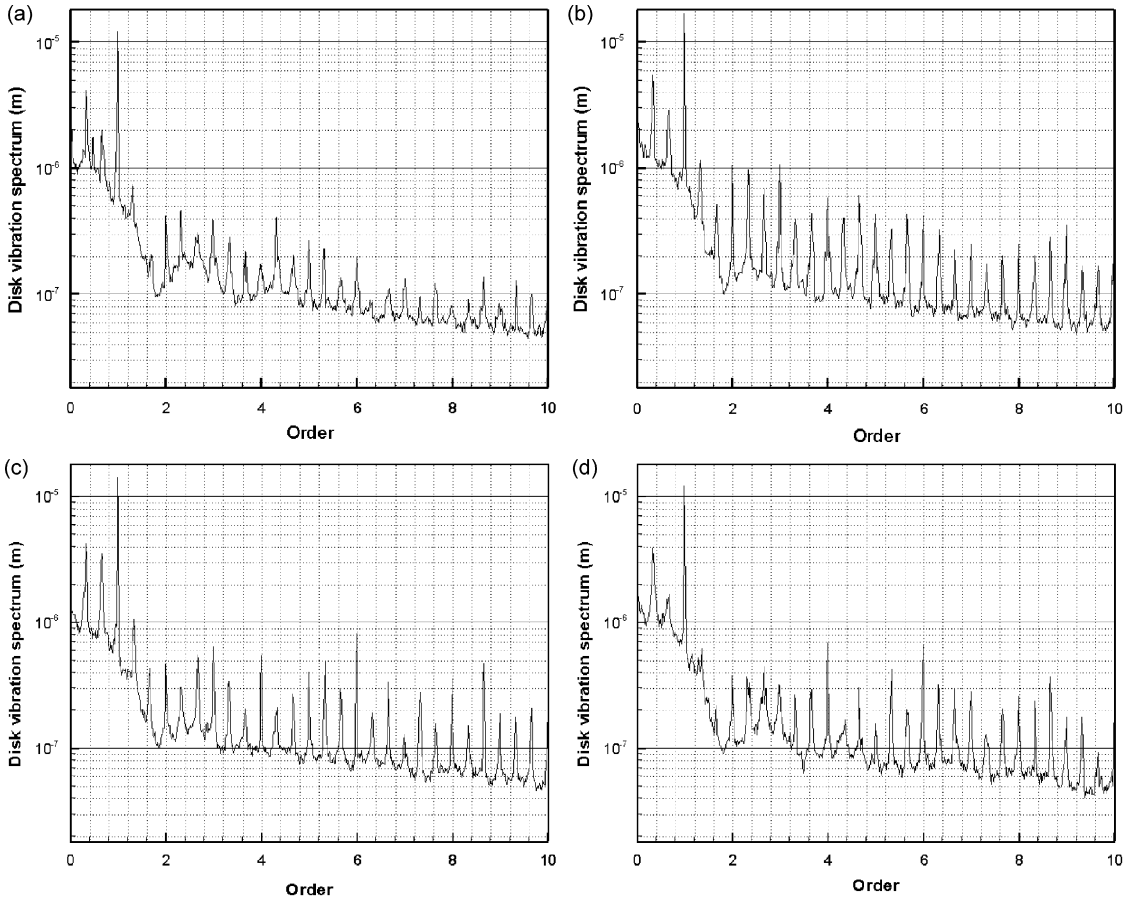

Fig. 13. Displacement response of ODD with different top covers at 4000 rev/min: (a) no cover, (b) Cover 1, (c) Cover 2 and (d) Cover 3.

Table 5
Disk displacement of the first three orders (unit: μm)

Rev/min	Order	Without cover	Cover 1	Cover 2	Cover 3
4000	1	12.1	16.71	14.05	12.00
	2	0.42	1.04	0.46	0.38
	3	0.39	1.06	0.63	0.31
6000	1	3.58	5.14	3.54	5.17
	2	0.44	0.45	0.15	0.76
	3	0.15	0.28	0.31	0.43
8000	1	1.31	0.78	0.28	0.23
	2	0.29	0.34	0.64	0.33
	3	0.16	0.11	0.18	0.27

the manuscript, the disk displacement response is represented using order spectra instead of frequency spectrum from direct FFT of a time signal in order to avoid smear caused by the unstable rotating speed. With Cover 2 and Cover 3, the amplitudes of the disk are significantly smaller than that with Cover 1 between the second and third orders. Notice that lots of small structural features are neglected in the model simplified from an ODD in order to speed up the time-consuming computation process of flow-induced vibration using the finite-element method. As a result, one may predict that a great difference exists in comparing the result

Table 6
Sound pressure level of the disk rotating at 8000 rev/min (unit: dB)

Order	Without cover	Cover 1	Cover 2	Cover 3
1	47.0	56.4	37.4	43.6
2	33.6	38.3	36.8	36.1
3	30.1	38.2	36.6	33.3

between the numerical analysis and experiment. However, the trend from both results seems to be correlated well by comparing Fig. 9 with Fig. 13 using the frequency information.

Altogether, the experiment and the numerical simulation reach the same conclusion that Cover 3 has a better performance in suppressing the vibration and noise of the rotating disk. It concludes that with a proper design of a disk cover, both the flow-induced disk vibration and the associate noise can be reduced.

7. Conclusions

Three top covers with different shapes of an optical disk drive have been designed to investigate the aerodynamic effect on the disk stability and the related noise from an ODD. Results show that the cover shape influences the velocity field of the rotating flow and then alters the characteristics of secondary recirculating vortex. Moreover, the coupling advection effects among streamlines affect the distribution of fluid pressure on the optical disk. All the effective pressure frequencies of three different top covers are close to the nature frequency corresponding to the first axisymmetric mode of the disk and leads to the disk self-excited vibration. Nevertheless, numerical simulations show that altering the shape can improve the disk response caused by the effective pressure substantially when compared to the original shape of the top cover. Furthermore, experimental results validate that the associate noise that includes the flow noise and structure-borne noise of disk can be reduced more than 10 dB at the same rotating speed. Eventually, an optimization procedure combined with the algorithm developed here seems to be feasible to determine the top cover shape that can stabilize the high-speed rotating disk. Moreover, tooling the top cover using a press seems to be cost-effective in a manufacturing process for practical applications.

Acknowledgments

This work was partially supported by Fu Sheng Co. and the National Science Council of Taiwan, Republic of China under Contract no. NSC 95-2221-E-194-061.

References

[1] R.C. Benson, D.B. Bogy, Deflection of a very flexible spinning disk due to a stationary transverse load, *Journal of Applied Mechanics* 45 (1978) 636–642.
[2] D.F. Torok, R. Gronseth, Flow and thermal fields in channels between corotating disks, *IEEE Transactions on Components, Hybrids, and Manufacturing Technology* 11 (4) (1988) 585–593.
[3] K. Yasuda, T. Torii, T. Shimizu, Self-excited oscillation of a circular disk rotating in air, *JSME International Journal* 35 (3) (1992) 347–352.
[4] S. Kim, G. Han, H. Son, A study of characteristics of disk vibration and rotating airflow in magneto optical disk drives, *IEEE Transactions on Consumer Electronics* 44 (3) (1998) 601–605.
[5] B.C. Kim, A. Raman, C.D. Mote Jr., Prediction of aeroelastic flutter in a hard disk drive, *Journal of Sound and Vibration* 238 (2) (2000) 309–325.
[6] H. Shimizu, M. Tokuyama, S. Imai, S. Nakamura, K. Sakai, Study of aerodynamic characteristics in hard disk drives by numerical simulation, *IEEE Transactions on Magnetics* 37 (2) (2001) 831–836.
[7] S. Imai, Fluid dynamics mechanism of disk flutter by measuring the pressure between disks, *IEEE Transactions on Magnetics* 37 (2) (2001) 837–841.
[8] C. D' Angelo III, C.D. Mote Jr., Aerodynamically excited vibration and flutter of a thin disk rotating at supercritical speed, *Journal of Sound and Vibration* 168 (1) (1993) 15–30.

[9] S.V. Patankar, D.B. Spalding, A calculation procedure for heat, mass and momentum transfer in 3-D parabolic flows, *International Journal of Heat and Mass Transfer* 15 (1972) 1787–1806.
[10] S.G. Hutton, S. Chonan, B.F. Lehmann, Dynamic response of s guided circular saw, *Journal of Sound and Vibration* 112 (3) (1987) 527–539.
[11] E.J. Hopfinger, *Rotating Fluid in Geophysical and Industrial Applications*, Springer, New York, 1992.
[12] A.J. Baker, *Finite Element Computational Fluid Mechanics*, Hemisphere Publishing Corporation, New York, 1983.
[13] S.S. Girimaji, Fully explicit and self-consistent algebraic Reynolds stress model, *Theoretical and Computational Fluid Dynamics* 8 (6) (1996) 387–402.
[14] D. Guo, F.L. Chu, The influence of rotation on vibration of a thick cylindrical shell, *Journal of Sound and Vibration* 242 (3) (2001) 487–505.
[15] A.N. Brooks, T.J.R. Hughes, Streamline upwind/Petro-Galkerin formulation for convection dominated flows with particular emphasis on the incompressible Navier–Stokes equations, *Computer Methods in Applied Mechanics and Engineering* 32 (1982) 199–259.
[16] S.H. Kim, The reduction of air-borne noise in hard disk drive, *Proceedings, Asia-Pacific Magnetic Recording Conference*, 2000, MP6/1–MP6/2.
[17] P. Kohnke, *ANSYS Theory Reference*, ninth ed., SAS IP, Inc., 1998.
[18] H. Schlichting, *Boundary Layer Theory*, McGraw-Hill, New York, 1968.